Journal of Pathology Informatics 15 (2024) 100354

Contents lists available at ScienceDirect

Journal of Pathology Informatics

journal homepage: www.elsevier.com/locate/jpi

A deep learning model to predict Ki-67 positivity in oral squamous cell carcinoma

Francesco Martino [a,b], Gennaro Ilardi [b], Silvia Varricchio [b], Daniela Russo [b], Rosa Maria Di Crescenzo [b], Stefania Staibano [b,1], Francesco Merolla [c,*]

[a] Dedalus HealthCare, Division of Diagnostic Imaging IT, Gertrude-Frohlich-Sandner-Straße 1, Wien 1100, Austria
[b] Department of Advanced Biomedical Sciences, University of Naples, Via Pansini, 5, Naples 80131, Italy
[c] Department of Medicine and Health Sciences "V. Tiberio", University of Molise, Via De Sanctis, Campobasso 86100, Italy

ARTICLE INFO

Keywords:
OSCC
Ki-67
Prediction
Deep learning

ABSTRACT

Anatomical pathology is undergoing its third revolution, transitioning from analogical to digital pathology and incorporating new artificial intelligence technologies into clinical practice. Aside from classification, detection, and segmentation models, predictive models are gaining traction since they can impact diagnostic processes and laboratory activity, lowering consumable usage and turnaround time. Our research aimed to create a deep-learning model to generate synthetic Ki-67 immunohistochemistry from Haematoxylin and Eosin (H&E) stained images. We used 175 oral squamous cell carcinoma (OSCC) from the University Federico II's Pathology Unit's archives to train our model to generate 4 Tissue Micro Arrays (TMAs). We sectioned one slide from each TMA, first stained with H&E and then re-stained with anti-Ki-67 immunohistochemistry (IHC). In digitised slides, cores were disarrayed, and the matching cores of the 2 stained were aligned to construct a dataset to train a Pix2Pix algorithm to convert H&E images to IHC. Pathologists could recognise the synthetic images in only half of the cases in a specially designed likelihood test. Hence, our model produced realistic synthetic images. We next used QuPath to quantify IHC positivity, achieving remarkable levels of agreement between genuine and synthetic IHC.

Furthermore, a categorical analysis employing 3 Ki-67 positivity cut-offs (5%, 10%, and 15%) revealed high positive-predictive values. Our model is a promising tool for collecting Ki-67 positivity information directly on H&E slides, reducing laboratory demand and improving patient management. It is also a valuable option for smaller laboratories to easily and quickly screen bioptic samples and prioritise them in a digital pathology workflow.

Introduction

The majority of artificial intelligence algorithms are designed to cover a wide range of possible applications in surgical pathology, such as cancer grading, classification, molecular subtyping, outcome prediction, and segmentation.[1–8]

AI applications for OSCC whole slide image (WSI) analysis are becoming popular.[9] Several AI-based feature approaches have been described in oral and oropharyngeal lesions.[10–19] Martino et al. described a machine learning approach to demonstrate the possibility of predicting Ki-67 immunohistochemistry positive on OSCC WSI.[20] Aside from traditional AI tasks, one of the hottest topics in the field of neural networks is the use of Generative Adversarial Networks (GAN), which are data-generating.[21] These model can be used for various data types, including image synthesis for data augmentation, super-resolution, Natural Language Processing (NLP), and music generation.[22] The Pix2Pix network is one of the most interesting examples of generative networks since it is easily adaptable to many purposes. It was first presented by Isola et al. at the Conference on Computer Vision and Pattern Recognition (CVPR) in 2017, and several applications have been proposed since then[23] Pix2Pix network has been proposed as a stain normalisation method, producing outstanding results,[24] and can be used to convert H&E stained slides to different stainings, as detailed by De Haan et al.[25] and Liu et al.[26] in 2021.

In keeping with our prior findings, we wanted to see how well a generative network might be used to assess Ki-67 in OSCCs.

The IHC labeling index (LI) of the Ki-67 nuclear protein, as determined by immunostaining with the MIB1 monoclonal antibody on formalin-fixed, paraffin-embedded (FFPE) tissue sections, is one of the most commonly used techniques in surgical pathology.[27,28] Scholzer and Gerdes discovered the Ki-67 antigen in the early 1980s, and it encodes two 345 kDa and 395 kDa isoforms.[29] Ki-67 protein expression is dependent on cell proliferation, is expressed in all cell cycle phases except G0, and can be employed

* Corresponding author.
E-mail address: francesco.merolla@unimol.it (F. Merolla).
[1] Co-senior author.

http://dx.doi.org/10.1016/j.jpi.2023.100354
Received 12 May 2023; Received in revised form 14 August 2023; Accepted 16 November 2023
Available online 22 November 2023

as a malignant tumour aggressiveness biomarker.[30,31] As a result, pathologists frequently use the Ki-67 labeling index as a proliferation marker.[32] Ki-67 has been proposed as a diagnostic biomarker in several tumours because it is overexpressed in malignant tumour tissues compared to normal ones,[33,34] and it correlates to tissue differentiation in an inversely proportional manner; many studies have shown a correlation between the Ki-67/MIB-1 labeling index and human cancer grading.[30,35–40] Furthermore, it correlates with the clinical tumours' stage and occult metastasis,[41–44] and Ki-67 expression evaluation, in combination with other histopathological characteristics, may also represent an indicator of the risk of tumour recurrence.[45,46] Ki-67 IHC labeling has been shown to have predictive value in a variety of human solid tumours, including breast, soft tissue, lung, prostate, cervix, and central nervous system.[47–51] Different ways to optimise the Ki-67 LI assessment by digital image analysis of Ki-67 IHC-stained glass slides have been offered. Still, none of them is focused on predicting Ki-67 IHC positive from an H&E (haematoxylin and eosin)-stained glass slide.[52,53] We collected 175 OSCC FFPE samples from the archives of the University of Naples "Federico II" Anatomical Pathology unit to develop a deep learning model to convert H&E stained whole slide images to anti-Ki-67 IHC-stained whole slide images to reduce turnaround time and laboratory consumables use, improving patient management, and helping to prioritise samples in a digital pathology workflow.

Results

Dataset generation

To generate a dataset of images of Ki-67 immunostained tumour samples perfectly matching the corresponding H&E, in the first instance, we generated 4 TMAs from a series of 175 OSCCs, sampling each tumour at least in duplicate to ensure we used at least one core for each tumour after quality control. Our TMAs, containing 349 cores, were stained with H&E and, after a destaining procedure, immunostained with anti-Ki67 antibody. Following a quality check step, the selected H&E and IHC-stained cores were manually aligned to create a high-quality matching-images dataset. Following a TMA dearray preprocessing, each IHC stained core was manually overlaid to the matching H&E, and the images were precisely aligned using Adobe Photoshop 2021 software. Then, the single layers (H&E and IHC) were saved as individual images, as shown in Fig. 1.

Then, cores were subdivided into tiles, and each Ki67 tile was concatenated to its H&E counterpart to create the actual training dataset, with some examples shown in Fig. 2.

Finally, images were sorted into 3 datasets: training, test, and validation, as described in materials and methods, and a Pix2Pix model was trained. As shown in Fig. 3, synthetic IHC images generated using the trained model appeared similar to actual immunostained images.

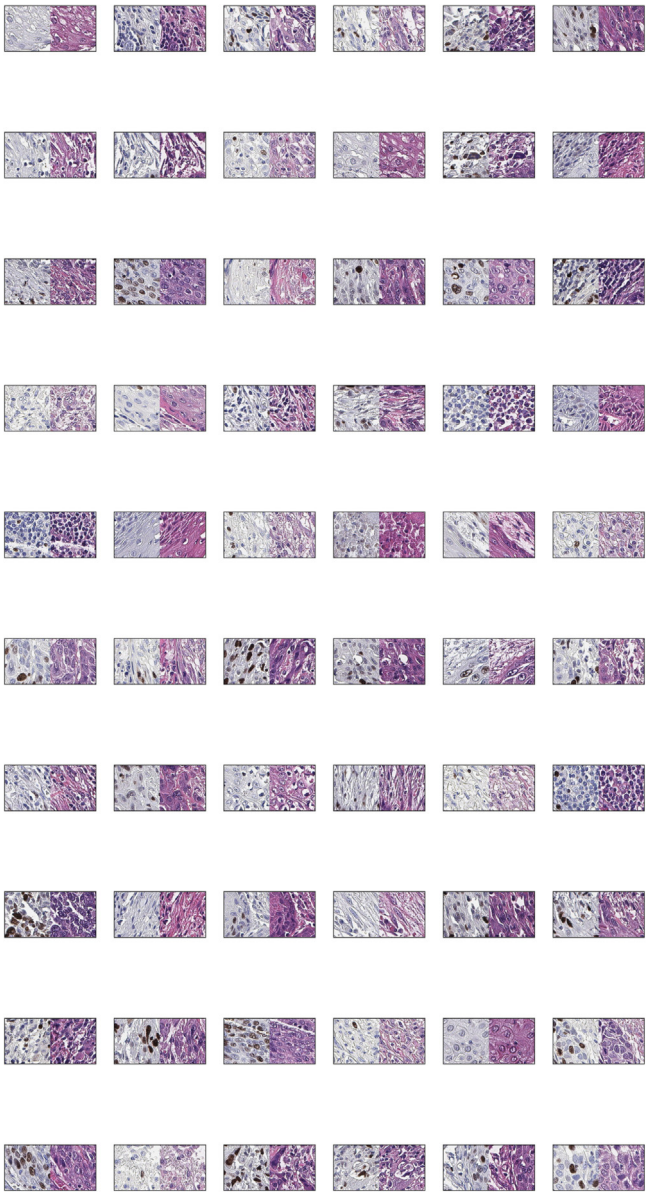

Fig. 2. A grid showing some representative images of tiles. Each couple is made of a target image (Ki67 immunohistochemistry, left) and an input image (H&E, right).

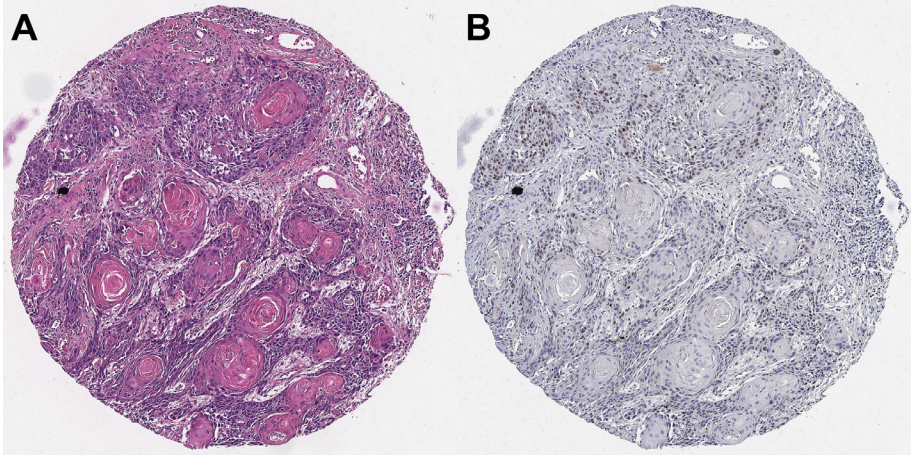

Fig. 1. A representative image of 2 aligned cores, with the H&E in (A) and the IHC in (B). Cores have been manually annotated to a pixel level.

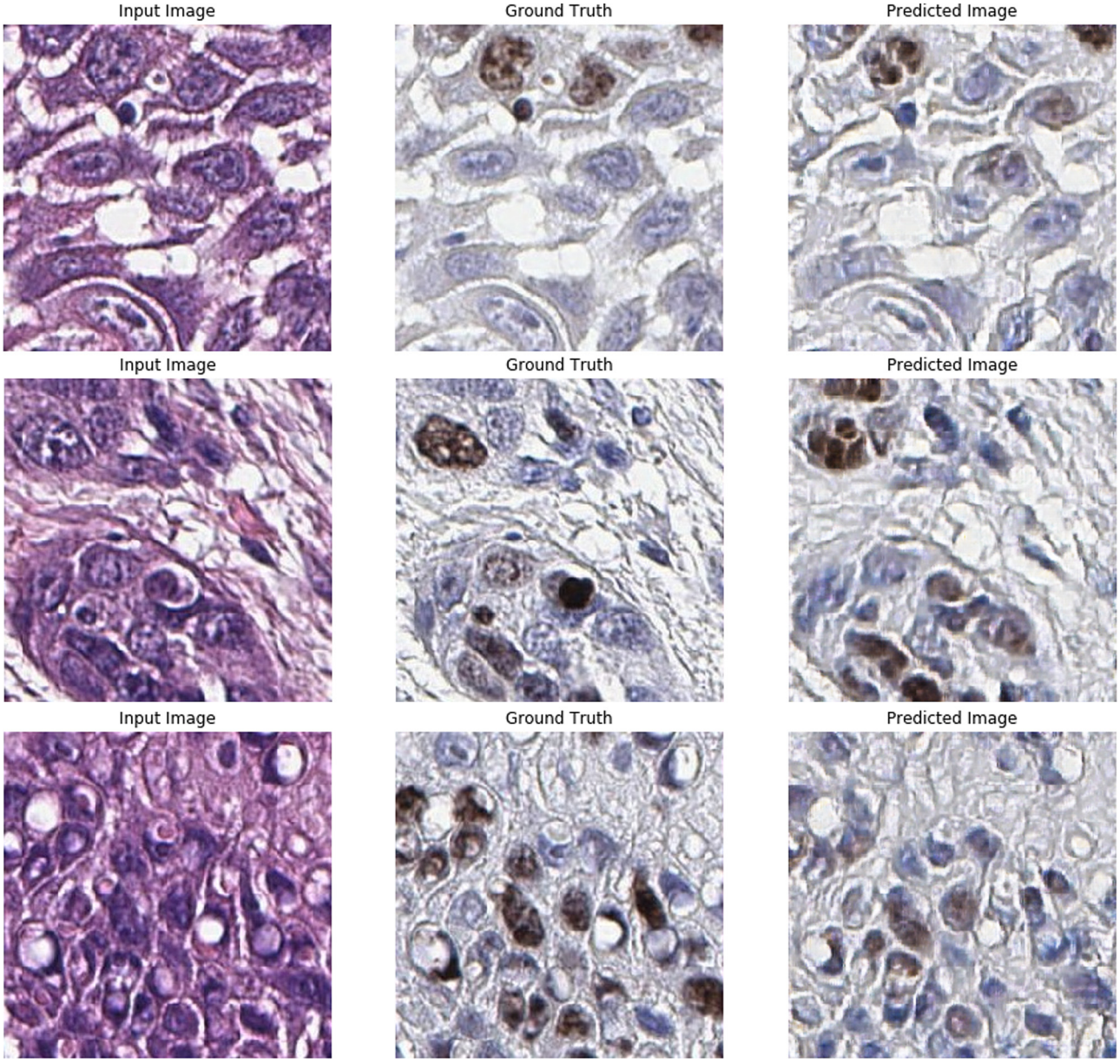

Fig. 3. Three representative images of the IHC prediction procedure. From left: Input H&E, Actual IHC, Synthetic IHC.

Synthetic images likelihood

As the proposed method generates virtual staining, the output should appear realistic. Indeed, pathologists are used to working with actual IHC images, so realistic images (other than accurate predictions) are mandatory to assure pathologists' compliance with the algorithm application. Hence, the likelihood of synthetic images was assessed by asking 2 pathologists to tell the synthetic image from the actual one in a side-by-side blinded comparison. The test was performed in a dedicated Android application with a user-friendly GUI, developed to allow a pathologist to evaluate model results (Fig. 4).

Synthetic image likelihood was measured as the percentage of synthetic images correctly identified as synthetic (True positives). Hence, a percentage of 0.5 means that the pathologist could not tell synthetic images from actual ones, while a value of 1 means that synthetic images are always recognisable. It resulted that out of 30 images, only 17 and 16 (Pathologist 1 and Pathologist 2) were correctly recognised as synthetic, with a mean ratio of 0.55 (0.57 and 0.53), confirming the likelihood of the images and the quality of the model (Table 1). Overall, these results confirm that the images produced by the model appear realistic, assuring more compliance and confidence from pathologists. Then, we quantitatively evaluated the immunohistochemical concordance between synthetic and actual images.

Synthetic and real IHC concordance

To assess the concordance between synthetic and real immunohistochemical concordance, we automatically counted the number of positive cells per each core using QuPath "Positive Cell detection" as described in Materials and Methods. The synthetic and real IHC comparison showed a moderate R^2 value (0.558), as shown in Fig. 5.

Moreover, the visual inspection of the digitally generated cores confirmed that the distribution pattern of positive cells matches the actual one, as shown in Fig. 6.

Finally, categorical division in the most commonly used cut-off in the assessment of Ki-67 showed a high accuracy rate. Indeed, when using a 5% positivity cut-off, we achieved an accuracy of 74.51%, with high sensitivity (76.67%) and specificity (71.43%). With a higher cut-off, we had a remarkable reduction in sensitivity, although we observed a remarkable

Fig. 4. Screenshots of the application developed to assess the likelihood of the model's output images.

Table 1
Out of 30 synthetic IHCs shown to Pathologist 1 and to Pathologist 2, only slightly more than 50% were correctly recognised as "virtual" IHC. in 13/30 and 14/30 cases, respectively, the Pathologists (P1 and P2) were unable to say if the picture they were looking at was true or synthetic.

	Wrong	Right	*% of misclassification*
P1	13	17	43.33%
P2	14	16	46.67%

positive-predictive value (79.31%, 77.78%, and 75.00%) (Table 2 and Fig. 7). A detailed list of metrics is reported in supplementary data (Supplementary Table S1). Although further studies are necessary to improve the algorithms and achieve a clinically applicable accuracy level, our results

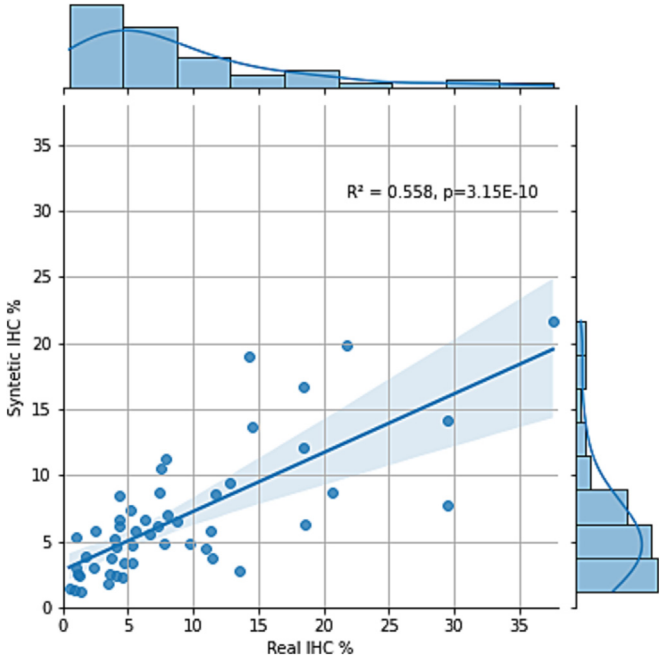

Fig. 5. Jointplot showing the correlation between the predicted number of share of IHC positive cells and the actual one.

paved the way for a promising and reliable tool to produce immunohistochemical images directly from H&E-stained slides.

Discussion

During the last 20 years, pathology underwent a radical transformation thanks to introduction of digital pathology, an innovative approach that merges computer science with pathology. In digital pathology, annotated datasets are crucial for machine- and deep-learning approaches. To date, few laboratories have gone "full digital" (i.e., employing a full digital workflow), despite this trend constantly increasing in recent years,[54,55] resulting in a lack of publicly available datasets and difficulties for research groups interested in developing new algorithms, severely limiting the development of artificial intelligence (AI) algorithms. However, with the exponential expansion of new accessible algorithms, more and more results are published yearly, and various applications have been proposed for less diffuse cancers, such as oral squamous cell carcinoma. The first computer science approaches proposed to surgical pathology regarded the automation of manual procedures as cell counts. However, with time, more and more algorithms have been developed, ranging from colour normalisation to automatic classification and segmentation of tumours. Nevertheless, one of the most outstanding applications of AI to pathology is the prediction of molecular or morphological characteristics through virtual staining. The expression "virtual staining" refers to the employment of AI to obtain synthetic images of a desired target staining (as IHC, Trichrome, or another staining) from a source image (as H&E) without the need for an actual laboratory activity and reducing the reagent consumption. Among the proposed algorithms, the prediction of immunohistochemistry is one of the most interesting topics because of the continuous increase in the number of tumoural biomarkers and the consequent impact on hospital budget and activity. Hence, we intended to develop an AI algorithm to predict the immunohistochemical positivity of Ki-67, a well-known proliferation marker related to a worse prognosis in several tumours.

We initially obtained 349 cores from the 175 OSCC cases selected to construct the 4 TMAs. We harvested at least 2 cores from each tumour. After a strict quality check phase, we selected 165 individual cores that were disarrayed and tiled to create our training, validation, and test set. The quality check allowed us to select the intact cores with the highest

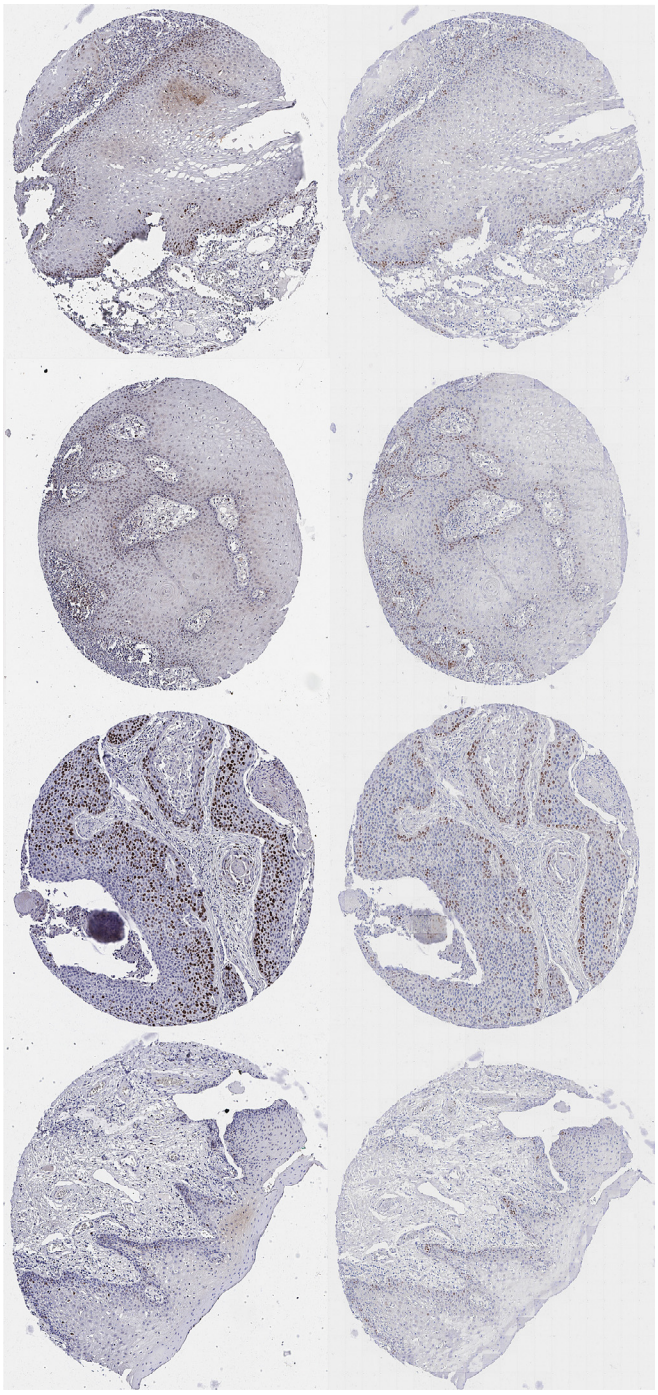

Fig. 6. A comparison between actual immunohistochemistry (left) and the respective virtual one (right). It is clearly visible a close match in positivity and its pattern.

tumour content, excluding those affected by cutting or staining artifacts. The workflow we conceived for constructing our model foresees a careful processing phase in the wet lab. The tumours in the series are all oral cavity squamous cell carcinomas, homogeneous in terms of anatomic site, morphology, and biological behavior (they are all advanced infiltrating squamous cell carcinomas). Most of the cores dropped by the process were duplicates. The Dataset obtained was representative of advanced infiltrating OSCC. We trained a Pix2Pix model to achieve virtual stained cores from H&E images. The obtained images were assessed for their likelihood to real ones at a tile-level, while concordance between real and synthetic Ki-67 immunohistochemical expression has been assessed at a core-level with continuous and categorical quantification through QuPath.

Table 2
Summary of model IHC concordance metrics.

Metric	5%	10%	15%
True positives	23	7	3
False positives	6	2	1
True negatives	15	33	42
False negatives	7	9	5
Sensitivity	76.67%	43.75%	37.50%
(95% CI)	(57.72%–90.07%)	(19.75%–70.12%)	(8.52%–75.51%)
Specificity	71.43%	94.29%	97.67%
(95% CI)	(47.82%–88.72%)	(80.84%–99.30%)	(87.71%–99.94%)
Accuracy	74.51%	78.43%	88.24%
(95% CI)	(60.37%–85.67%)	(64.68%–88.71%)	(76.13%–95.56%)

Virtual images deceived pathologists in 45% of cases, confirming the likelihood of the generated images. Moreover, the synthetic and real IHC positivity, measured using QuPath algorithms, showed a highly significant concordance ($R^2 = 0.56$, $P < .001$). In some cases, risk stratification is done by categorising the case based on the percentage of neoplastic cells positive for the marker. Therefore, we have chosen to test the agreement metrics between real and synthetic IHC by analysing the differences across 3 percentage cut-offs (Table S1). Ki-67 is assessed as a low-high expression, although the cut-off value is still not defined and usually ranges between 5% and 15% of positive cells. Hence, we assessed the concordance with 3 cut-offs (5%, 10%, and 15%) and achieved a remarkable positive-predictive value of 79.31%, 77.78%, and 75.00%, respectively, confirming the algorithm's quality.

As heterogeneity is a well-known issue with Ki67 testing, we also tested the model on full sections WSIs, other than TMA cores. As shown in supplementary data (Fig. S1), obtained results are aligned with our TMA findings. We also cross-checked the reproducibility of the virtual Ki-67 expression in cases of weak or moderate-intensity IHCs. Fig. S2 shows representative images from model output (IHC groud truths and relative predictions) subjected to QuPath positive cell count script as described in the Materials and Methods section. We also asked whether our model could be adopted for Ki-67 assessment of other tumours, such as breast carcinoma. Supplementary Fig. S3 shows the result of the Ki67-IHC prediction. As expected, the prediction does not reach satisfactory results compared to breast Ki67-IHC ground truth (Fig. S4). To obtain a more generalisable model, the creation of extensive and heterogeneous datasets would be required, which is the subject of our interest for a forthcoming publication.

Overall, our results confirm the feasibility of a valid IHC-prediction algorithm, even with the limitation of our study. Indeed, we performed our training on TMA cores, which were made with samples collected in a different time period and then with an intrinsic variability in IHC staining. Moreover, we used a relatively small amount of OSCC cores, all coming from our institute, so further studies are necessary to assess the generalisability of our algorithm. In conclusion, although larger and wider studies are necessary to fine-tune and improve our algorithm, our results represent a promising starting point to develop further a virtual staining protocol to reduce the turnaround time and the material and reagents consumption to achieve an actual *digital* pathology. Virtual staining protocols may result, in the future, in a faster and more economical way to gather information about protein expression and mutational status of patients, improving the effectiveness of therapies and also in small hospitals or developing countries as they can usually hardly access immuno-stainers, reagent supplies, and adequate trained stuff, enabling high-level patient-care requiring only a slide scanner, and limited computer hardware to run the algorithms.

Methods

Study population and tissue slides preparation

175 OSCC FFPE OSCC tumour samples from surgical resections were retrieved from the Pathology Unit's archive of the University of Naples "Federico II". They were used to build 4 tissue microarrays (TMAs), and the most representative areas from each selected paraffin block were

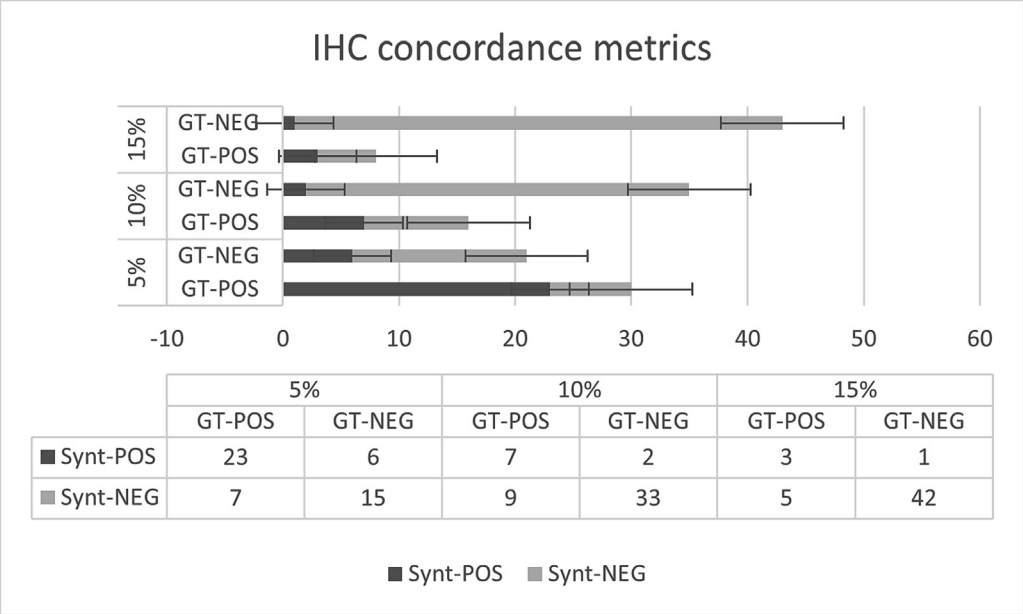

	5%		10%		15%	
	GT-POS	GT-NEG	GT-POS	GT-NEG	GT-POS	GT-NEG
Synt-POS	23	6	7	2	3	1
Synt-NEG	7	15	9	33	5	42

Fig. 7. The histogram shows the concordance metrics between synthetic IHC results compared to ground truth (GT). The cut-off groups results. Error bars show the standard error.

selected at least in duplicate. TMAs were built and stained as described in Martino et al.,[20] and 349 individual cores were obtained. H&E stained TMA slides were scanned using a Leica Aperio AT2 scanner with a 40× magnifier. After slide scanning, TMAs slide coverslips were removed by soaking the slides in xylene. The slides were then rehydrated in decreasing ethanol concentrations and then destained using a solution of HCl 0.3% for 4 min. After destaining, the slides were rinsed in tap water and immunostained with the antibody anti-Ki-67. Immunohistochemical staining was performed on a Ventana Benchmark Ultra (Ventana Medical Systems Inc., Tucson, AZ, USA) using the rabbit monoclonal antibody anti-Ki-67 (clone 30-9, Ventana Medical Systems Inc.) following manufacturers' recommendations. The new IHC-stained slides were then digitised.

Dataset generation

All the 349 individual cores for both H&E and IHC images were disarrayed using QuPath,[56] and the matching cores were manually aligned to achieve a nearly perfect pixel-to-pixel correspondence. After a strict quality check phase, which led to the discharge of 184 cores, the 165 remaining cores were sorted into 3 different datasets, training (approximately 60% of cores), test (10%), and validation (30%). Because of the experiment's nature, the algorithm's validation has been performed by measuring the verisimilitude of the generated images and the concordance between real and synthetic images. As each core is, on average, 4500 × 4500 pixels, they have been tiled, obtaining 31 428, 6109, and 16 560 tiles for each dataset. Validation cores were reassembled to obtain virtual cores. A summary of the datasets is illustrated in Table 3. While the scheme in Fig. 8 illustrates the laboratory workflow from the selection of patients to the staining of histological slides up to the generation of datasets and the model building.

Pix2Pix implementation

A Pix2Pix model has been trained on the training and test dataset to convert H&E images into anti-Ki-67 immunostained images for 30 epochs using the default settings as described by Isola et al.[23] In particular, the model consists of the discriminator and the generator. During the training, the generator is trained to generate synthetic IHC images, while the discriminator is trained to tell synthetic images from the actual ones. In our training, we used an Adam optimiser with a learning rate of 2×10^{-4} and a momentum of 0.5 for both generator and optimiser, while the random initialiser has been set with a mean of 0 and a standard deviation of 0.02. The model has been trained using 2 GPU Nvidia 2080 Ti. For each epoch, we saved a checkpoint and restored the best generative model at the end of the training. A validation set has been used to assess the model efficiency in 2 ways. In the first place, we tested the ability of 2 pathologists to discern actual images from synthetic ones on a small subset of the validation set to evaluate the likelihood of synthetic images. Then, we counted positive cells for each core (both actual and synthetic) to evaluate the concordance between real Ki-67-positivity and the predicted one.

Table 3
Cores and tiles distribution in train, validation, and test set. Tiles are 256 × 256 patches extracted from 4500 × 4500 cores images

	Train	Test	Validation
Cores	95	19	51
Tiles	31 428	6109	16 560

IHC quantification

Immunopositivity has been measured using QuPath 0.2.3. After setting the image type and defining stains (H&E, DAB, and background) values, the Simple Tissue Detector has been used to define tissue areas in the images. Then, we used the "Positive cell detection" algorithm to detect and quantify positive cells within the core, and the procedure was automated using a Groovy script (Code 1). As IHC intensity is sometimes highly variable, the positivity threshold has been manually adjusted for some cores.

```
//QuPath Groovy S c r i p t
// Simple Tissue Detector
run Plugin ('qupath.imagej.detect.tissue. Simple Tissue Detection 2',
'{"threshold": 220 ,
"requestedDownsample": 50.0,
"min Area Pixels": 100000.0,
```

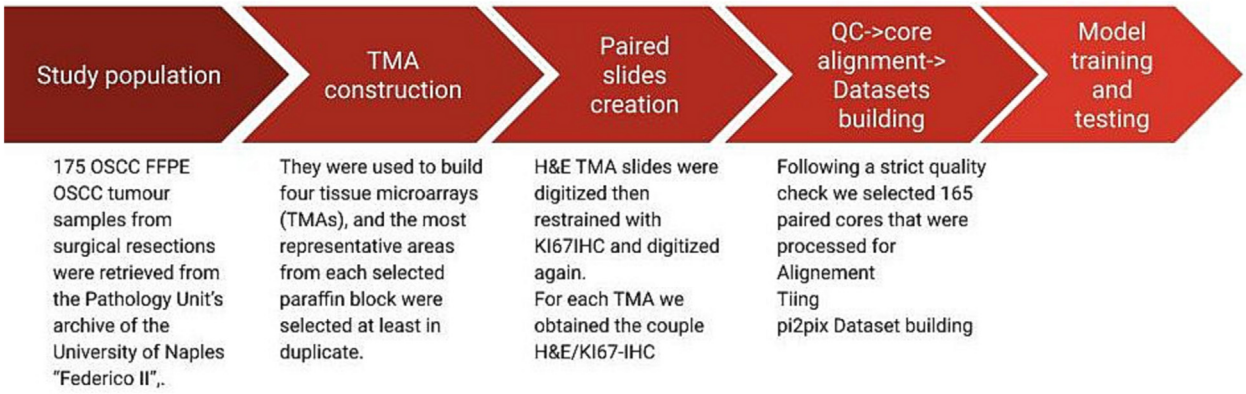

Fig. 8. The scheme illustrates the laboratory workflow from the selection of patients to the staining of histological slides up to the generation of datasets and model building.

```
"max Hole Area Pixels": 500.0,
"darkBackground": false,
"smoothImage": true,
"medianCleanup": true,
"dilate Boundaries": false,
"smooth Coordinates": true,
"excludeOnBoundary": false,
"single Annotation": true }');

// Positive Cell Detection
run Plugin ('qupath.imagej.detect.cells. Positive Cell Detection',
'{ "detection Image Brightfield": "Optical density sum",
"background Radius": 15.0,
"medianRadius": 6.0,
"sigma": 6.0,
"minArea": 10.0,
"maxArea": 1000.0,
"threshold": 0.1,
"maxBackground": 2.0,
"watershed Post Process": true,
"excludeDAB": false,
"cell Expansion": 0.0,
"include Nuclei": true,
"smooth Boundaries": true,
"makeMeasurements": true,
"threshold Compartment": "Nucleus: DAB OD mean",
"threshold Positive 1": 0.2,
"threshold Positive 2": 0.4,
"threshold Positive 3": 0.6000000000000001,
"single Threshold": true }');
```

Listing 1. QuPath Groovy script to perform tissue detection and cell positivity count.

Android application

An Android application has been developed to test the likelihood of synthetic images. The test shows a series of coupled IHC images, A and B, and the pathologists had to identify the synthetic one by clicking on the relative button. On each trial, the pathologist was shown each image for 5 s, after which the pictures disappeared, and unlimited time to respond as to which was fake was given. Each session consisted of a brief trial to understand the functioning of the application, followed by the actual survey. The experimental setting has been adapted from the one used by Isola et al.[23] The application is made of 3 activities: (I) Main Activity, (II) Trial Activity, and (III) Survey Activity.

Main activity. The Main Activity is composed of 3 buttons, namely "Trial", "Survey", and "Settings", respectively, linking to the activities and a setting menu. The setting menu allows to activate/deactivate the hiding of the images and a timer, along with the number of images for each session. Setting values were saved as SharedPreferences.

Trial activity. The Trial Activity is made of a disclaimer about the survey with an explanation of the modality, the actual test, and feedback. The trial starts by clicking the "Start" button in the disclaimer, and 3 images are shown to test the application. At the end of the test, feedback is provided.

Survey activity. The Survey Activity is an exact copy of the trial one but shows several images as fixed in settings. We showed 30 images to each pathologist.

The resulting application has been installed on an Android tablet, and the pathologist has been supported only during the trial phase.

Code and statistical analysis

All code and statistical analysis has been performed using Python 3.9 with the packages Seaborn 0.11.1, Matplotlib 3.4.2, Pandas 1.3.0, Scikit-learn 0.241.2, OpenCv 4.5.3.56, and Tensorflow 2.6.0. The Android application has been developed using Kotlin with Android Studio. All codes are available upon request.

Author contributions statement

F.Ma. and F. Me. conceived the experiment(s), F.Ma. conducted the experiment(s), G.I. and S.V. F.Ma.,

S.S and F. Me. analysed the results. All authors reviewed the manuscript.

Declaration of Competing Interest

The author(s) declare no competing interests.

Acknowledgements

This study was supported by POR Campania FESR 2014-2020 grant; "Technological Platform: eMORFORAD-Campania" grant PG/2017/0623667.

Appendix A. Supplementary data

Supplementary data to this article can be found online at https://doi.org/10.1016/j.jpi.2023.100354.

References

1. Tian K, Rubadue CA, Lin DI, et al. Automated clear cell renal carcinoma grade classification with prognostic significance. PLoS One 2019;14(10). https://doi.org/10.1371/journal.pone.0222641.
2. Xu H, Park S, Hwang TH. Computerized classification of prostate cancer gleason scores from whole slide images. IEEE/ACM Trans Computat Biol Bioinform 2019;17(6). https://doi.org/10.1109/tcbb.2019.2941195.
3. Jaber MI, Song B, Taylor C, et al. A deep learning image-based intrinsic molecular subtype classifier of breast tumors reveals tumor heterogeneity that may affect survival. Breast Cancer Res 2020;22(1). https://doi.org/10.1186/s13058-020-1248-3.
4. Tang Z, Chuang KV, DeCarli C, et al. Interpretable classification of Alzheimer's disease pathologies with a convolutional neural network pipeline. Nat Commun 12, 2019;10. https://doi.org/10.1038/s41467-019-10212-1.
5. Guo Z, Liu H, Ni H, et al. A fast and refined cancer regions segmentation framework in whole-slide breast pathological images. Scient Rep 12, 2019;9. https://doi.org/10.1038/s41598-018-37492-9.
6. Nielsen FS, Pedersen MJ, Olsen MV, Larsen MS, Røge R, Jørgensen AS. Automatic bone marrow cellularity estimation in h&e stained whole slide images. Cytometry Part A 2019;95:1066–1074. https://doi.org/10.1002/cyto.a.23885.
7. Bueno G, Fernandez-Carrobles MM, Gonzalez-Lopez L, Deniz O. Glomerulosclerosis identification in whole slide images using semantic segmentation. Comput Methods Prog Biomed 2, 2020;184. https://doi.org/10.1016/j.cmpb.2019.105273.
8. Martino F, Bloisi DD, Pennisi A, et al. Deep learning-based pixel-wise lesion segmentation on oral squamous cell carcinoma images. Appl Sci 2020;10(22):8285.Publisher: Multidisciplinary Digital Publishing Institute: https://doi.org/10.3390/app10228285.
9. Mahmood H, Shaban M, Indave BI, Santos-Silva AR, Rajpoot N, Khurram SA. Use of artificial intelligence in diagnosis of head and neck precancerous and cancerous lesions: a systematic review. Oral Oncol 2020;110, 104885. https://doi.org/10.1016/j.oraloncology.2020.104885.
10. Sun Y-N, Wang Y-Y, Chang S-C, Wu L-W, Tsai S-T. Color-based tumor tissue segmentation for the automated estimation of oral cancer parameters. Microsc Res Tech 2009;73. https://doi.org/10.1002/jemt.20746.
11. Rahman TY, Mahanta LB, Chakraborty C, Das AK, Sarma JD. Textural pattern classification for oral squamous cell carcinoma. J Microsc 2018;269:85–93. https://doi.org/10.1111/jmi.12611.
12. Fouad S, Randell D, Galton A, Mehanna H, Landini G. Unsupervised morphological segmentation of tissue compartments in histopathological images. PLoS One 2017;12, e0188717. https://doi.org/10.1371/journal.pone.0188717.
13. Das DK, Bose S, Maiti AK, Mitra B, Mukherjee G, Dutta PK. Automatic identification of clinically relevant regions from oral tissue histological images for oral squamous cell carcinoma diagnosis. Tissue Cell 2018;53:111–119. https://doi.org/10.1016/j.tice.2018.06.004.
14. Baik J, Ye Q, Zhang L, et al. Automated classification of oral premalignant lesions using image cytometry and random forests-based algorithms. Cell Oncol 2014;37. https://doi.org/10.1007/s13402-014-0172-x.
15. Krishnan MMR, Venkatraghavan V, Acharya UR, et al. Automated oral cancer identification using histopathological images: a hybrid feature extraction paradigm. Micron 2012;43. https://doi.org/10.1016/j.micron.2011.09.016.
16. Krishnan MMR, Shah P, Chakraborty C, Ray AK. Statistical analysis of textural features for improved classification of oral histopathological images. J Med Syst 2012;36:865–881. https://doi.org/10.1007/s10916-010-9550-8.
17. Krishnan MMR, Choudhary A, Chakraborty C, Ray AK, Paul RR. Texture based segmentation of epithelial layer from oral histological images. Micron 2011;42. https://doi.org/10.1016/j.micron.2011.03.003.
18. Krishnan MMR, Pal M, Bomminayuni SK, et al. Automated classification of cells in subepithelial connective tissue of oral sub-mucous fibrosis-an svm based approach. Comput Biol Med 2009;39:1096–1104. https://doi.org/10.1016/j.compbiomed.2009.09.004.
19. Mookiah MRK, Shah P, Chakraborty C, Ray AK. Brownian motion curve-based textural classification and its application in cancer diagnosis. Anal Quant Cytol Histol 2011;33:158–168.
20. Martino F, Varricchio S, Russo D, et al. A machine-learning approach for the assessment of the proliferative compartment of solid tumors on hematoxylin-eosin-stained sections. Cancers 2020;12. https://doi.org/10.3390/cancers12051344.
21. Goodfellow I, Pouget-Abadie J, Mirza M, et al. Generative adversarial nets. In: *Ghahramani Z, Welling M, Cortes C, Lawrence N, Weinberger KQ, eds. Advances in Neural Information Processing Systems.* Curran Associates, Inc; 2014. https://proceedings.neurips.cc/paper/2014/file/5ca3e9b122f61f8f06494c97b1.
22. Gui J, Sun Z, Wen Y, Tao D, Ye J. A Review on Generative Adversarial Networks: Algorithms, Theory, and Applications. arXiv:2001.06937 [cs, stat]ArXiv: 2001.06937. Jan, 2020.
23. Isola P, Zhu J-Y, Zhou T, Efros AA. Image-to-image translation with conditional adversarial networks. arXiv 2018.arXiv:1611.07004.
24. Salehi P, Chalechale A. Pix2pix-based stain-to-stain translation: a solution for robust stain normalization in histopathology images analysis. arXiv 2020. arXiv:2002.00647.
25. de Haan K, Zhang Y, Zuckerman JE, et al. Deep learning-based transformation of H&E stained tissues into special stains. Nat Commun 2021;12(1):4884. https://doi.org/10.1038/s41467-021-25221-2.
26. Liu S, Zhang B, Liu Y, et al. Unpaired stain transfer using pathology-consistent constrained generative adversarial networks. IEEE Trans Med Imaging 2021;40(8):1977–1989. https://doi.org/10.1109/TMI.2021.3069874.
27. Gerdes J, Schwab U, Lemke H, Stein H. Production of a mouse monoclonal antibody reactive with a human nuclear antigen associated with cell proliferation. Int J Cancer 1983;31(1):13–20. https://doi.org/10.1002/ijc.2910310104.
28. Cattoretti G, Becker MHG, Key G, et al. Monoclonal antibodies against recombinant parts of the Ki-67 antigen (MIB 1 and MIB 3) detect proliferating cells in microwave-processed formalin-fixed paraffin sections. J Pathol 1992;168(4):357–363. https://doi.org/10.1002/path.1711680404.
29. Scholzen T, Gerdes J. The Ki-67 protein: from the known and the unknown. J Cell Physiol 2000;182(3):311–322. https://doi.org/10.1002/(SICI)1097-4652(200003)182:3¡311::AID-JCP1¿3.0.CO;2-9.
30. Kloppel G, Perren A, Heitz PU. The gastroenteropancreatic neuroendocrine cell system and its tumors: the WHO classification. Ann NY Acad Sci 2004;1014(1):13–27. https://doi.org/10.1196/annals.1294.002.
31. Brown DC, Gatter KC. Ki67 protein: the immaculate deception?: Ki67 protein. Histopathology 2002;40(1):2-11. https://doi.org/10.1046/j.1365-2559.2002.01343.x.
32. Spyratos F, Ferrero-Poüs M, Trassard M, et al. Correlation between MIB-1 and other proliferation markers: clinical implications of the MIB-1 cutoff value. Cancer 2002;94(8):2151–2159. https://doi.org/10.1002/cncr.10458.
33. Claudio PP, Zamparelli A, Garcia FU, et al. Expression of cell-cycle-regulated proteins pRb2/p130, p107, p27(kip1), p53, mdm-2, and Ki-67 (MIB-1) in prostatic gland adenocarcinoma. Clin Cancer Res Off J Am Assoc Cancer Res 2002;8(6):1808–1815.
34. Hu H-Y, Liu H, Zhang J-W, Hu K, Lin Y. Clinical significance of Smac and Ki-67 expression in pancreatic cancer. Hepato-Gastroenterol 2012;59(120):2640–2643. https://doi.org/10.5754/hge12071.
35. Kim JY, Hong S-M, Ro JY. Recent updates on grading and classification of neuroendocrine tumors. Ann Diagnost Pathol 2017;29:11–16. https://doi.org/10.1016/j.anndiagpath.2017.04.005.
36. Lind-Landstrom T, Habberstad AH, Sundstrøm S, Torp SH. Prognostic value of histological features in diffuse astrocytomas WHO grade II. Int J Clin Exp Pathol 2012;5(2):152–158.
37. Kim B-h, Bae Y-s, Kim SH, Jeong H-j, Hong SW, Yoon SO. Usefulness of Ki-67 (MIB-1) immunostaining in the diagnosis of pulmonary sclerosing hemangiomas. APMIS Acta Pathol Microbiol Immunol Scand 2013;121(2):105–110. https://doi.org/10.1111/j.1600-0463.2012.02945.x.
38. Kloppel G, La Rosa S. Correction to: Ki67 labeling index: assessment and prognostic role in gastroenteropancreatic neuroendocrine neoplasms. Virchows Archiv Int J Pathol 2018;472(3):515. https://doi.org/10.1007/s00428-017-2283-z.
39. Nabi U, Nagi AH, Sami W. Ki-67 proliferating index and histological grade, type and stage of colorectal carcinoma. J Ayub Medical Coll Abbottabad: JAMC 2008;20(4):44–48.
40. Inwald EC, Klinkhammer-Schalke M, Hofstadter F, et al. Ki-67 is a prognostic parameter in breast cancer patients: results of a large population-based cohort of a cancer registry. Breast Cancer Res Treat 2013;139(2):539–552. https://doi.org/10.1007/s10549-013-2560-8.
41. McCormick D, Chong H, Hobbs C, Datta C, Hall PA. Detection of the Ki-67 antigen in fixed and wax-embedded sections with the monoclonal antibody MIB1. Histopathology 2002;41(3A):173–178. https://doi.org/10.1046/j.1365-2559.2002.14891.x.
42. Merkel DE, Dressler LG, McGuire WL. Flow cytometry, cellular DNA content, and prognosis in human malignancy. J Clin Oncol Off J Am Soc Clin Oncol 1987;5(10):1690–1703. https://doi.org/10.1200/JCO.1987.5.10.1690.
43. Clark GM, Mathieu MC, Owens MA, et al. Prognostic significance of S-phase fraction in good-risk, node-negative breast cancer patients. J Clin Oncol Off J Am Soc Clin Oncol 1992;10(3):428–432. https://doi.org/10.1200/JCO.1992.10.3.428.
44. Fernandez EB, Sesterhenn IA, McCarthy WF, Mostofi FK, Moul JW. Proliferating cell nuclear antigen expression to predict occult disease in clinical stage I nonseminomatous testicular germ cell tumors. J Urol 1994;152(4):1133–1138. https://doi.org/10.1016/s0022-5347(17)32522-3.
45. Morimoto R, Satoh F, Murakami O, et al. Immunohistochemistry of a proliferation marker Ki67/MIB1 in adrenocortical carcinomas: Ki67/MIB1 labeling index is a predictor for recurrence of adrenocortical carcinomas. Endocr J 2008;55(1):49–55. https://doi.org/10.1507/endocrj.k07-079.
46. Lu L, Wan X, Xu Y, Chen J, Shu K, Lei T. Prognostic factors for recurrence in pituitary adenomas: recent progress and future directions. Diagnostics (Basel, Switzerland) 2022;12(4):977. https://doi.org/10.3390/diagnostics12040977.
47. Ishihara M, Mukai H, Nagai S, et al. Retrospective analysis of risk factors for central nervous system metastases in operable breast cancer: effects of biologic subtype and Ki67 overexpression on survival. Oncology 2013;84(3):135–140. https://doi.org/10.1159/000345321.
48. Sorbye SW, Kilvaer TK, Valkov A, et al. Prognostic impact of CD57, CD68, M-CSF, CSF-1R, Ki67 and TGF-beta in soft tissue sarcomas. BMC Clin Pathol 2012;12:7. https://doi.org/10.1186/1472-6890-12-7.
49. Sorbye SW, Kilvaer TK, Valkov A, et al. Prognostic impact of Jab1, p16, p21, p62, Ki67 and Skp2 in soft tissue sarcomas. PLoS One 2012;7(10), e47068. https://doi.org/10.1371/journal.pone.0047068.
50. Ciancio N, Galasso MG, Campisi R, Bivona L, Migliore M, Di Maria GU. Prognostic value of p53 and Ki67 expression in fiberoptic bronchial biopsies of patients with non small cell lung cancer. Multidisc Resp Med 2012;7(1):29. https://doi.org/10.1186/2049-6958-7-29.
51. Josefsson A, Wikstrom P, Egevad L, et al. Low endoglin vascular density and Ki67 index in Gleason score 6 tumours may identify prostate cancer patients suitable for surveillance. Scand J Urol Nephrol 2012;46(4):247–257. https://doi.org/10.3109/00365599.2012.669791.
52. Bengtsson E, Ranefall P. Image analysis in digital pathology: combining automated assessment of Ki67 staining quality with calculation of Ki67 cell proliferation index. Cytometry Part A J Int Soc Anal Cytol 2019;95(7):714–716. https://doi.org/10.1002/cyto.a.23685.
53. Acs B, Pelekanou V, Bai Y, et al. Ki67 reproducibility using digital image analysis: an inter-platform and inter-operator study. Lab Investig J Techn Methods Pathol 2019;99(1):107–117. https://doi.org/10.1038/s41374-018-0123-7.

54. Betmouni S. Diagnostic digital pathology implementation: Learning from the digital health experience. Digital Health 2021;7. https://doi.org/10.1177/20552076211020240.20552076211020240.
55. Fraggetta F, L'Imperio V, Ameisen D, et al. Best practice recommendations for the implementation of a digital pathology workflow in the anatomic pathology laboratory by the European Society of Digital and Integrative Pathology (ESDIP). Diagnostics (Basel, Switzerland) 2021;11(11):2167. https://doi.org/10.3390/diagnostics11112167.
56. Bankhead P, Loughrey MB, Fernandez JA, et al. QuPath: open source software for digital pathology image analysis. Scient Rep 2017;7(1):16878. https://doi.org/10.1038/s41598-017-17204-5.